The Astronomical Journal, 159:175 (17pp), 2020 April https://doi.org/10.3847/1538-3881/ab79a5

ExoRel$^{\mathfrak{R}}$: A Bayesian Inverse Retrieval Framework for Exoplanetary Reflected Light Spectra

Mario Damiano[1] and Renyu Hu[1,2]
[1] Jet Propulsion Laboratory, California Institute of Technology, Pasadena, CA 91109, USA; mario.damiano@jpl.nasa.gov
[2] Division of Geological and Planetary Sciences, California Institute of Technology, Pasadena, CA 91125, USA
Received 2019 September 12; revised 2020 January 27; accepted 2020 February 22; published 2020 March 30

Abstract

The high-contrast imaging technique is meant to provide insight into those planets orbiting several astronomical units from their host star. Space missions such as *Wide-Field InfraRed Survey Telescope*, *Habitable Exoplanet Imaging Mission*, and *Large Ultra-Violet/Optical/InfraRed Surveyor* will measure reflected light spectra of cold gaseous and rocky planets. To interpret these observations, we introduce ExoRel$^{\mathfrak{R}}$ (Exoplanetary Reflected Light Retrieval), a novel Bayesian retrieval framework to retrieve cloud properties and atmospheric structures from exoplanetary reflected light spectra. As a unique feature, it assumes a vertically nonuniform volume mixing ratio (VMR) profile of water and ammonia, and uses it to construct cloud densities. In this way, clouds and molecular mixture ratios are consistent. We apply ExoRel$^{\mathfrak{R}}$ on three test cases: two exoplanets (υ And e and 47 Uma b) and Jupiter. We show that we are able to retrieve the concentration of methane in the atmosphere, and estimate the position of clouds when the signal-to-noise ratio of the spectrum is higher than 15, in line with previous works. Moreover, we described the ability of our model to give a chemical identity to clouds, and we discussed whether or not we can observe this difference in the planetary reflection spectrum. Finally, we demonstrate how it could be possible to retrieve molecular concentrations (water and ammonia in this work) below the clouds by linking the nonuniform VMR profile to the cloud presence. This will help to constrain the concentration of water and ammonia unseen in direct measurements.

Unified Astronomy Thesaurus concepts: Planetary science (1255); Planetary atmospheres (1244); Bayesian statistics (1900); Exoplanets (498); Extrasolar gas giants (509); Radiative transfer (1335); Spectroscopy (1558)

1. Introduction

The diversity observed in the thousands of exoplanets present nowadays in our catalog has extended the horizon of our knowledge of the dynamical, physical, and chemical properties of these alien worlds. This has mostly been made possible by characterizing their atmospheres. Focusing on the gaseous-giant planets population, the majority of them are made of hydrogen and helium. Therefore, the relevant questions concern the amounts of elements other than hydrogen and helium, i.e., the heavy elements, that are present. The atmospheres of short-period gaseous planets (these are generally hot or warm), Jupiter- and Neptune-sized, have been observed. The emission and transmission spectra have revealed molecular absorption of H_2O, CO, CH_4, CO_2, TiO, and VO (Swain et al. 2008, 2009; Snellen et al. 2010; Fraine et al. 2014; Evans et al. 2016; Sing et al. 2016; Damiano et al. 2017, 2019; Tsiaras et al. 2018) and in some cases the presence of clouds and hazes in the atmosphere (Berta et al. 2012; Knutson et al. 2014; Sing et al. 2016; Barstow et al. 2017; Tsiaras et al. 2018). The transit technique has provided most of the current results, as it benefits more from target planets being close to their parent stars. However, these planets show a different environment compared to the scenario emerging from the studies conducted in our solar system planets due to higher irradiation received (Burrows et al. 1997; Karkoschka 1998; Seager & Sasselov 1998).

The high-contrast imaging technique is poised to provide insight into those planets orbiting several astronomical units from their host star so that their equilibrium temperature is low enough to let different chemical and dynamical behavior emerge (e.g., condensation mechanism, cold trap effects, etc.) with respect to their better-studied hot counterparts. This technique has been successfully tested in studies of star- and planet-forming regions (Barman et al. 2011; Skemer et al. 2014; Macintosh et al. 2015). Future direct-imaging exoplanet space mission and mission concepts, e.g., *Wide-Field InfraRed Survey Telescope* (*WFIRST*; Spergel et al. 2013, 2015), *Habitable Exoplanet Imaging Mission* (*HabEx*; Mennesson et al. 2016), *Large Ultra-Violet/Optical/InfraRed Surveyor* (*LUVOIR*; Peterson & Fischer 2017), and Starshade rendezvous probe,[3] will have the opportunity to observe the starlight reflected by exoplanets via high-contrast imaging and also to unveil their atmospheric structure. Rayleigh scattering, molecular absorption, and scattering and absorption by atmospheric condensates determine the reflection spectra of gaseous exoplanets (Marley et al. 1999; Seager et al. 2000). Clouds, if present in the atmosphere, are the primary factor that controls the appearance of an exoplanet. Previous studies have shown that the presence and formation of the clouds are regulated by atmospheric temperature (Sing et al. 2016; Barstow et al. 2017). Assuming an atmospheric elemental abundance the same as the Sun and a suitable atmospheric temperature (~200–300 K), gaseous-giant exoplanets may have ammonia, water, or silicate clouds in their atmospheres (Sudarsky et al. 2000, 2003; Burrows et al. 2004). The radiative properties of the clouds are sensitive to the vertical extent and density of the cloudy layers and the sizes of cloud particles (Ackerman & Marley 2001). The elemental abundance of the atmosphere also affects the formation of the clouds (Cahoy et al. 2010). For these reasons, reflected light spectra of exoplanets contain rich information on the composition and dynamic processes of the exoplanetary

[3] https://smd-prod.s3.amazonaws.com/science-red/s3fs-public/atoms/files/Starshade2.pdf

atmosphere. In the wavelength range 0.4–1.0 μm, where reflection spectroscopy mostly operates, it is possible to probe the molecular signatures of methane, ammonia, and water vapor (Burrows 2014; Hu 2014; Marley et al. 2014) along with their relative condensates. For example, the Jupiter reflection spectrum (e.g., Karkoschka 1998) contains different levels of methane absorption that have been used to reject simple models of a single reflective cloud deck, favoring a more complex double-layer cloud structure (Sato & Hansen 1979).

To interpret a spectrum and extrapolate information from it, a comparison between the observed data and the proposed model should be performed through a statistical inverse modeling. While several transmission and emission spectra inverse retrieval frameworks have been developed and established (e.g., Irwin et al. 2008; Madhusudhan & Seager 2009; Benneke & Seager 2012; Waldmann et al. 2015a, 2015b), reflected light spectroscopic retrieval models, to date, have just started to be explored. Several models have been proposed (e.g., Lupu et al. 2016; Feng et al. 2018; Batalha et al. 2019), but these models use optical properties of clouds (optical depth, scattering albedo, and asymmetry factor) as free model parameters without bounding them to a physical model of the cloud structure (e.g., particle size and chemical cloud identity).

In this work, we present ExoRel$^{\Re}$ (Exoplanetary Reflected Light Retrieval), a novel inverse retrieval framework based on a modified version of ExoRel (Hu 2019), which is a cloud formation and radiative transfer model to synthesize the wavelength dependence of the albedo (and therefore planetary flux) of a gaseous planetary atmosphere. ExoRel$^{\Re}$ uses a non-constant volume mixing ratio (VMR) vertical profile of water and ammonia as an input to compute the density and particle size of water and ammonia clouds, as well as a T-P profile consistent with the lapse-rate equation. This algorithm is used as forward model for the Bayesian sampler *nested sampling* (Skilling 2004, 2006; Sivia & Skilling 2006) and its implementation MultiNest (Feroz & Hobson 2008; Feroz et al. 2009, 2019; Buchner et al. 2014) to perform inverse retrieval processes on reflected light spectra.

The parameters adopted in this work are consistent with the gas-giant-exoplanets scenario that have equivalent orbital distances of 1–6 au around nearby F-G-K stars. Moreover, we adopted a spectral resolution of $R = 70$ for our tests (similar to the *WFIRST* detector spectral resolution), to explore the reflection spectra of giant exoplanets at 0.4–1.0 μm except for the Jupiter case (Section 5), which has been studied with a spectral resolution of $R = 120$. Results and settings of this work are also generally applicable to future direct-imaging mission concepts as they will be sensitive to similar regimes of planetary parameters.

In this paper, we describe our model and the basic concept behind reflection spectroscopy. We provide insight on the Bayesian analysis, and we present and discuss the results. The manuscript is organized as follows: In Section 2, we provide details of ExoRel$^{\Re}$. In particular, we discuss the atmospheric structure model, free-parameter space, and details related to the retrieval settings. In Section 3, we provide insights on the impact that each free parameter has on the albedo spectrum and, therefore, on the planetary reflected flux. In Sections 3.4 and 3.5, we show some of the implications of the setup adopted in this work. In Section 4, we explore the performance and the ability of our model to retrieve information from different scenarios by applying it to two exoplanetary test cases (υ And e in Section 4.1 and 47 Uma b in Section 4.2). In Section 5, we report the results of the analysis of the albedo of Jupiter (Section 5). In Section 6, we discuss the results obtained and the implications introduced by this novel model. Finally, in Section 7, we summarize the key points of the paper and discuss the future development of ExoRel$^{\Re}$.

2. ExoRel$^{\Re}$

2.1. Amended Forward Model

The forward model that synthesizes the planetary geometric albedo and the reflection spectrum is a modified version of the self-consistent ExoRel model presented in Hu (2019). In particular, in ExoRel, the atmosphere is divided into layers, and in each of these, the saturation point of water and ammonia in the gas phase is checked. If one or both reaches the saturation, the humidity is calculated, and the relative VMR vertical profile decreases accordingly. The amount subtracted from the VMR is then used to calculate the physical and optical properties of the clouds.

In ExoRel$^{\Re}$, we wanted to preserve this causal relationship defined in Hu (2019), but we also wanted the flexibility to change parameters to obtain a different atmospheric structure. Therefore, we "reverse-engineered" the process by directly defining a nonuniform VMR profile for water and ammonia to be used as a trigger for the calculation of the respective clouds properties. We do not consider the saturation point; rather, we use four free parameters that uniquely define each VMR profile (Figure 1 left panel).

The forward model can synthesize either the albedo at a specific phase angle or the planet/star contrast ratio. In this work, we focus on the albedo at a specific phase angle (hereafter referred to simply as "albedo") as proof of concept. We fix the phase angle to $\alpha = 60^{\circ}$ for the synthesized examples (Sections 3 and 4) and to the one reported in Karkoschka (1994) for the Jupiter example (Section 5). For the retrieval process, choosing to synthesize the albedo makes the gravity of the planet less significant as a free parameter, which, instead, is important if the planet/star contrast ratio is the quantity to be retrieved (see Section 3.1).

2.2. Free-parameter Space

We chose to design the free-parameter space to include general/observable features. For this reason, we did not include the single scattering albedo ($\bar{\omega}$), the asymmetry factor ($\bar{g}$), or the optical depth (τ) within our free parameters (Lupu et al. 2016; Batalha et al. 2019). These parameters are calculated self-consistently from other parameters since the clouds are linked to a physical model. The parameters space counts at a maximum 10 parameters when both water and ammonia condensates are considered. Four parameters are used to determine the VMR vertical profile of the water and four more describe the ammonia profile. As mentioned in Section 2.1, we define the following free parameters for each molecular VMR vertical profile:

1. the VMR of the molecule below the respective cloud layers;
2. the $P_{\rm top}$ as the altitude in terms of pressure, where the top layer of the cloud is present;

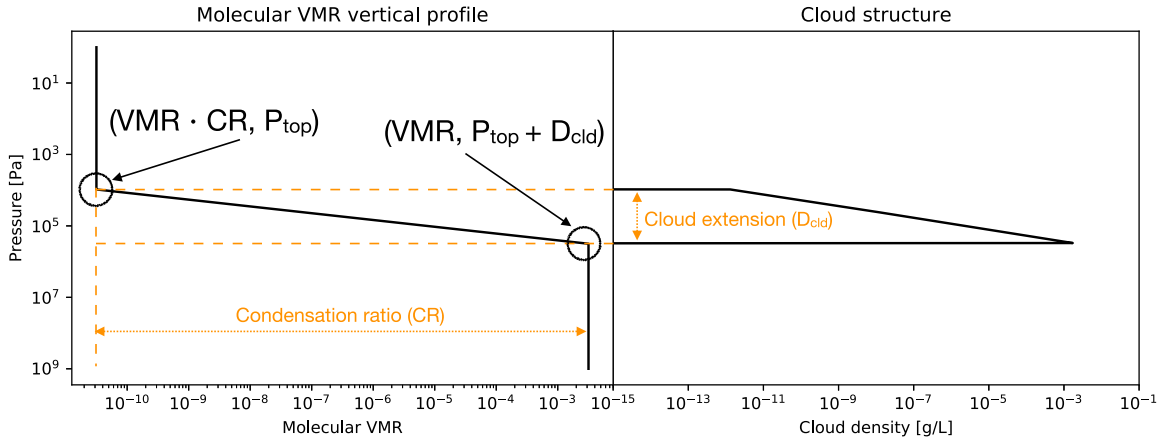

Figure 1. Left panel: the molecular vertical profile. In this work, we refer to it as water or ammonia. Where the drop of molecular VMR occurs, the cloud is present to compensate. Right panel: vertical profile of the cloud density relative to the VMR profile in the left panel.

3. the vertical extension of the cloud ($D_{\rm cld}$), which quantifies (in terms of difference) how much the cloud extends downwards from the $P_{\rm top}$;
4. the condensation ratio (CR), which accounts for the ratio between the leftover water in the gaseous form above the cloud and the molecular VMR below it.

The vertical profiles of water and ammonia are defined on a pressure grid spanning from 10^1 to 10^9 Pa, from top to bottom (see Figure 1 left panel). Moving upwards, the VMR could drop due to condensation of the relative molecular species. The drop is modeled as a linear decrease in logarithmic space. The number of layers where the VMR drops is regulated by the $P_{\rm top}$ and $D_{\rm cld}$. The VMR drop is then defined as

$$\mathrm{Log}(\Delta X) = \frac{\mathrm{Log}(X_{\rm bot}) - \mathrm{Log}(X_{\rm bot} \times \mathrm{CR})}{N_{\rm layers}} \quad (1)$$

where $N_{\rm layers}$ is the number of layers between $P_{\rm top}$ and $P_{\rm bot}$, and X is the VMR. The four free parameters, previously mentioned, uniquely define the molecular vertical profile. This assumption does not create appreciable differences with the proper and consistent calculation of the cloud density profile presented in Hu (2019). The right panel of Figure 1 shows the cloud relative to the defined molecular VMR vertical profile shown in the left panel. According to Hu (2019), the cloud density is calculated as follows:

$$\rho_{\rm cld} = \frac{\Delta X_i \mu P_i}{R T_i} \quad (2)$$

where ΔX_i is the VMR difference between two consecutive layers, μ is the molecular mean weight of the atmosphere, P_i and T_i are, respectively, the pressure and the temperature of the relative layer, and R is the gas constant.

Finally, the remaining two parameters are the VMR of the methane (considered constant) and the gravity acceleration of the planet.

A few challenges of the model used in this work arise from the assumptions of the model itself. The configuration used (see Section 2) implies that the clouds are water or ammonia purely; however, this is not always the case. In the case of Jupiter, for example, the ammonia clouds are not solely made of ammonia, photochemical hazes are present, and their influence can also be appreciated in the bluest part of the reflection spectrum (Weidenschilling & Lewis 1973; Sato & Hansen 1979; Karkoschka 1994, 1998). Since the model does not include the effects of hazes yet, we did not include the data points below 0.6 μm of the Jupiter albedo in our retrieval exercise (see Section 5). We can also expect that other cold gaseous exoplanets may have photochemical hazes in their atmosphere. It is crucial, then, to include the effects of hazes to obtain the best realistic scenario.

In light of the mechanism of this model, other condensable species (e.g., NH_4SH and CH_4) have to be included, so that other cold gaseous planet scenarios can also be addressed (e.g., Neptune-like planets).

2.3. MULTINEST Settings

The MULTINEST algorithm (Skilling 2004, 2006; Sivia & Skilling 2006; Feroz & Hobson 2008; Feroz et al. 2009, 2019; Buchner et al. 2014) is an established and robust method in the analysis of free-parameter space to recognize correlations and the best parameter values for a model. Among its qualities, MULTINEST is designed to better handle multimodal posteriors. Unlike Monte Carlo Markov Chain algorithms, MULTINEST can better avoid getting stuck into a local minimum. Moreover, the calculation of the Bayesian evidence is already included in the MULTINEST algorithm. This evidence allows us to generalize the Occams razor: a theory with compact parameter space (i.e., simpler) will have larger evidence than a more complicated one unless the latter is significantly better at explaining the data. We implemented this concept in our model by calculating the Bayesian factor, $\mathcal{B}$ to determine which between two models ($\mathcal{M}_1$ and $\mathcal{M}_2$) better represents the data. The Bayesian factor has been calculated as follows (Trotta 2008):

$$\mathcal{B}_{\frac{\mathcal{M}_1}{\mathcal{M}_2}} = \frac{\mathcal{P}(\mathcal{M}_1|\mathcal{D})}{\mathcal{P}(\mathcal{M}_2|\mathcal{D})} = \frac{\mathcal{Z}_1}{\mathcal{Z}_2}\frac{\mathcal{P}(\mathcal{M}_1)}{\mathcal{P}(\mathcal{M}_2)} \quad (3)$$

where $\mathcal{Z}$ is the total Bayesian evidence of the model and $\mathcal{D}$ represents the data. Generally, we would assume that $\mathcal{M}_1$ and $\mathcal{M}_2$ are equally likely. For this reason, the ratio $\frac{\mathcal{P}(\mathcal{M}_1)}{\mathcal{P}(\mathcal{M}_2)}$ is irrelevant for the determination of which model is better for the data. The choice is only related to the total evidence of the Bayesian sampling of the two models.

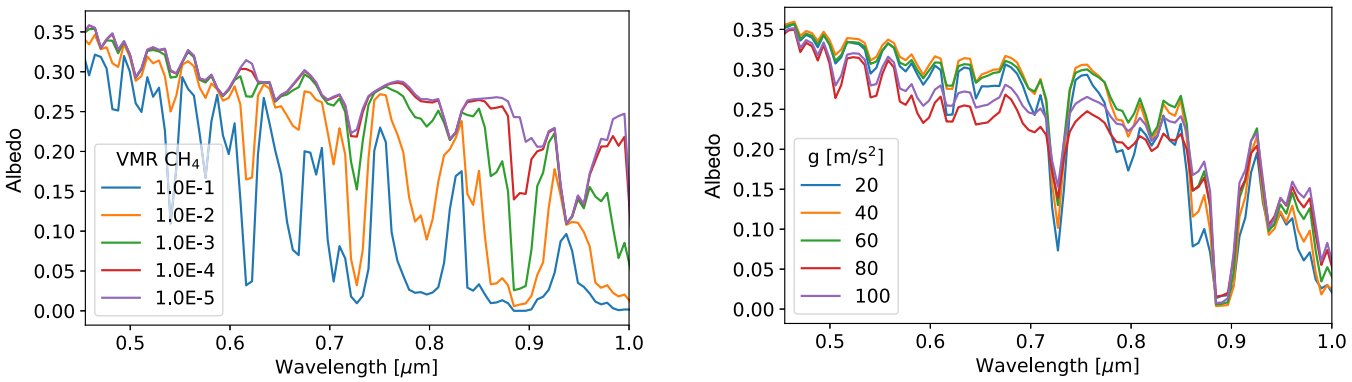

Figure 2. Left panel: the effect on the albedo due to the variation of the concentration of molecular methane in the atmosphere. Right panel: the variation of the planetary reflectivity produced by different gravity value. For these graphs, the following parameters have been adopted: $\log(\mathrm{VMR}_{\mathrm{H_2O}}) = -2.5$, $\log(\mathrm{VMR}_{\mathrm{NH_3}}) = -3.4$, $\log(P_{\mathrm{top,H_2O}}\ [\mathrm{Pa}]) = 4.0$, $\log(\mathrm{D}_{\mathrm{cld,H_2O}}\ [\mathrm{Pa}]) = 5.5$, and $\log(\mathrm{CR}_{\mathrm{H_2O}}) = -8.0$, $\log(P_{\mathrm{top,NH_3}}\ [\mathrm{Pa}]) = 3.0$, $\log(\mathrm{D}_{\mathrm{cld,NH_3}}\ [\mathrm{Pa}]) = 3.60$, and $\log(\mathrm{CR}_{\mathrm{NH_3}}) = -8.0$, and where applicable $\log(\mathrm{VMR}_{\mathrm{CH_4}}) = -2.8$, $g = 50\ \mathrm{m\ s^{-2}}$. The spectral resolution is $R = 70$ and the phase angle is $\alpha = 60°$.

Table 1
Priors for Each Scenario for the MultiNest Algorithm

Parameter	Cloud Models		
	Water	Ammonia	Two-cloud
$\mathrm{Log}(\mathrm{VMR}_{\mathrm{H_2O}})$	[−12, 0]	[−12, 0]	[−12, 0]
$\mathrm{Log}(\mathrm{VMR}_{\mathrm{NH_3}})$	[−12, 0]	[−12, 0]	[−12, 0]
$\mathrm{Log}(\mathrm{VMR}_{\mathrm{CH_4}})$	[−12, 0]	[−12, 0]	[−12, 0]
$\mathrm{Log}(P_{\mathrm{top,H_2O}})$	[0, 9]	⋯	[0, 8]
$\mathrm{Log}(D_{\mathrm{cld,H_2O}})$	[0, 9]	⋯	[0, 8.5]
$\mathrm{Log}(\mathrm{CR}_{\mathrm{H_2O}})$	[−12, 0]	⋯	[−12, 0]
$\mathrm{Log}(P_{\mathrm{top,NH_3}})$	⋯	[0, 9]	[0, 8]
$\mathrm{Log}(D_{\mathrm{cld,NH_3}})$	⋯	[0, 9]	[0, 8.5]
$\mathrm{Log}(\mathrm{CR}_{\mathrm{NH_3}})$	⋯	[−12, 0]	[−12, 0]
g	[10, 100]	[10, 100]	[10, 100]

For the MultiNest algorithm, we choose a Gaussian as likelihood function (i.e., the standard choice). The priors for all possible scenarios implemented in the algorithm are listed in Table 1. The choice of priors is fundamental for our scope, as they reflect our initial knowledge of the problem. For this reason, the priors have been defined uniformly among the ranges in Table 1 to give the same probability to all possible values. Moreover, the ranges have been defined to be large enough not to influence the final result of the Bayesian sampling (Skilling 2004, 2006; Sivia & Skilling 2006).

Note that in the case of the two-cloud model, the P_{top} of the deeper cloud (in ExoRel$^{\mathfrak{R}}$ the water cloud is always below the ammonia one) is instead defined relative to the bottom of the upper cloud and not to the top of the atmosphere. In this way, the two clouds are always separated and well distinguished.

3. Impact of Parameters on the Planetary Albedo Spectrum

3.1. $\mathrm{VMR}_{\mathrm{CH_4}}$ and g

In the wavelength range 400–1000 nm, there are numerous methane absorption bands (see Figure 2 left panel). The concentration of CH_4 affects the depth of these absorption bands. In the left panel of Figure 2, the clouds have been located at low altitude to show the methane molecular bands. The absorption can be severe with a high concentration of CH_4.

Gravity plays a weaker role in the calculation of the albedo. Mostly, it affects the shape and depth of molecular features. For the planet studied through high-contrast imaging, we assume to know the mass of the planet, so the gravity will give us information about the radius of the planet. Note that the effect of gravity will be better appreciated when the planetary flux or the planet/star contrast ratio is retrieved, instead of the albedo, as it depends directly on the planetary radius.

3.2. P_{top}, D_{cld}, and CR

P_{top}, D_{cld}, and CR are the parameters that, together with the molecular VMR, uniquely define the cloud density vertical profile (see Section 2.2 and Figure 1).

P_{top} regulates the vertical position of the cloud, and the effects on the planetary reflectivity can be seen in the top left panel of Figure 3. When the cloud is located high in the atmosphere (low pressure), the cloud density is not high enough to let the cloud be completely opaque. In this regime, light passes through, and the resultant reflectivity is weak. While P_{top} increases (moving down in the atmosphere), the cloud is denser as the reflectivity increases. However, if the cloud is too deep, the molecular absorption (mostly CH_4) is predominant and the albedo shows deep absorption bands.

D_{cld} affects the extension of the cloud in the atmosphere, and it represents the vertical depth from P_{top}. While all other parameters are kept fixed, the cloud depth affects the cloud density, and the layer where the optical depth reaches unity ($P_{\tau=1}$). If the cloud depth is small, it means that the cloud is quite thin, letting most of the light through and resulting in low scattering and strong molecular absorption. While the cloud extends further into the atmosphere, the cloud density increases, and the cloud can scatter more light back to the space. At the same time, $P_{\tau=1}$ moves down and molecular absorption features emerge as more column abundance is present on top of the cloud.

Since P_{bot} is calculated as the sum of P_{top} and D_{cld}, one of the two values may dominate the other; for this reason, we expect long tails in the posterior distribution that are not necessary related to the physics of the scenario, and each case has to be carefully considered.

The CR regulates the gradient of the cloud density from the top to the bottom of the cloud. The overall effect on the albedo is not significant, but it is useful to describe the vertical structure of the cloud. Moreover, it regulates the concentration of water and ammonia in the gas phase on top of the clouds, affecting the absorption of such molecules.

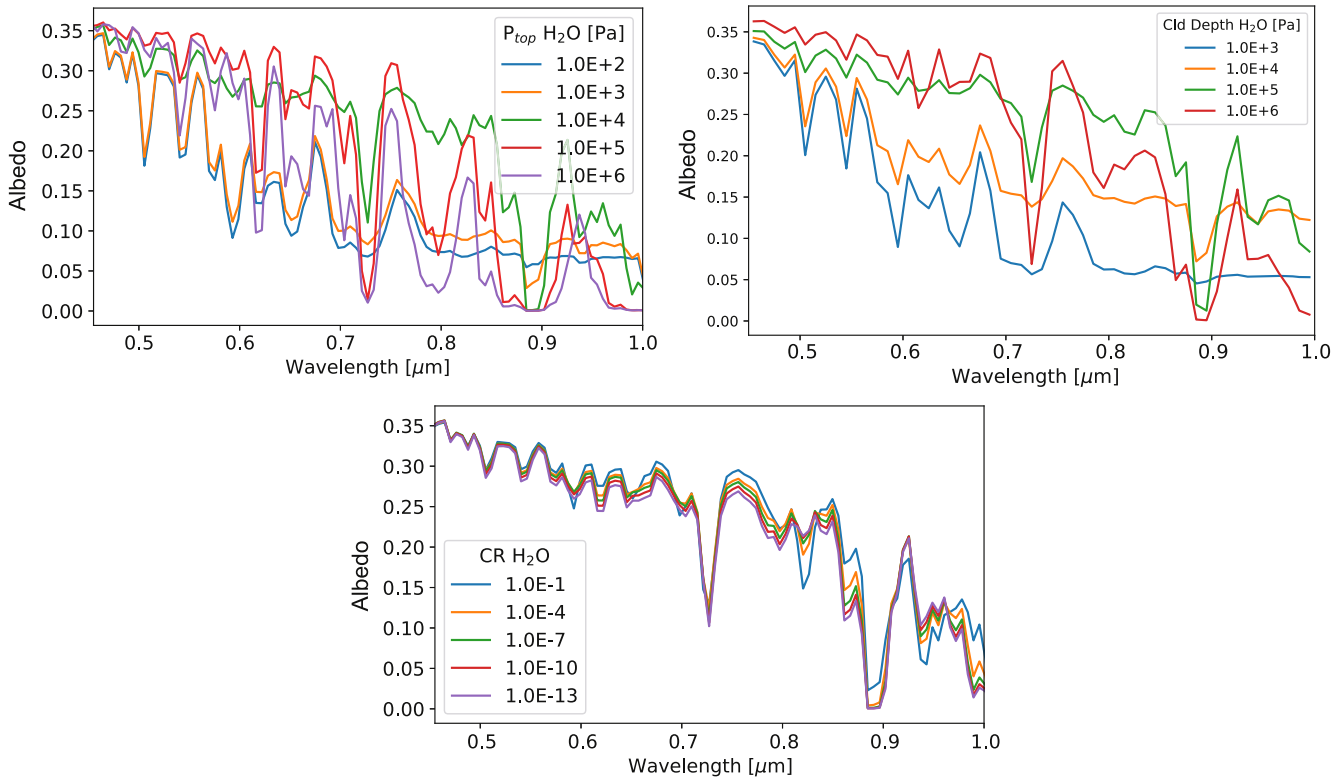

Figure 3. Top left panel: the effects of the variation of the albedo due to the $P_{\rm top}$. Top right panel: the variation of the planetary reflectivity produced by different cloud thicknesses. Bottom panel: the albedo in relation to the condensation ratio. The behavior of these parameters on ammonia clouds is similar. For these graphs, the following parameters have been adopted: $\log(\mathrm{VMR}_{\mathrm{H_2O}}) = -2.5$, $\log(\mathrm{VMR}_{\mathrm{NH_3}}) = -3.4$, $\log(\mathrm{VMR}_{\mathrm{CH_4}}) = -2.8$, $g = 50$ m s^{-2}, and where applicable $\log(P_{\rm top}$ [Pa]) =4.0, $\log(D_{\rm cld}$ [Pa]) = 5.5, and log(CR) = −8.0. The spectral resolution is $R = 70$ and the phase angle is $\alpha = 60°$.

3.3. $\mathrm{VMR}_{\mathrm{H_2O}}$ and $\mathrm{VMR}_{\mathrm{NH_3}}$

Even though we are not able to directly measure the molecular VMR below the cloud, its effect can still be observed in the total reflectivity of the planet. The molecular VMR is directly linked to the cloud density; the higher the concentration of that molecule, the greater the amount of material that can condense. For both ammonia and water, the behavior is indeed similar, low spectral continuum with a lower VMR and high continuum with higher VMR (see Figure 4 and Section 3.4).

To calculate the albedos shown in Figure 4, we tried to isolate the sole effect of the VMR to the planetary albedo. Other self-consistently calculated parameters such as the optical depth, however, may have affected the result. In the following section, we show a test case where the pressure level of the optical depth equal to unity has been kept constant while changing some of the other parameters.

The impact of the H_2O VMR has previously been explored on atmospheric reflected spectra (MacDonald et al. 2018). Also in their work, MacDonald et al. (2018) suggested that VMR H_2O signatures impact the height of clouds and the continuum of the albedo.

3.4. Probing Deep Down into the Atmosphere

EXOREL$^{\mathfrak{R}}$ has been designed to reflect some key concepts explained in Weidenschilling & Lewis (1973) and Sato & Hansen (1979). Our clouds are not opaque from the top layer downward, and they are not semi-infinite clouds; rather, they are finite and located in altitude. In our radiative transfer code, we perform calculations to a maximum optical depth value of $\tau_{\rm max} = 1000$. By adopting this strategy, we can model photons that are absorbed or scattered by regions of the atmosphere where $\tau > 1$. This gives the possibility of modeling the bottom part of the atmosphere. By taking into account the relation between the vertical VMR with the cloud structure (see Equations (1) and (2)) defined in this model, we may be able to recover the molecular VMR of some trace gasses before the depletion due to the condensation.

Figure 5 shows a test case. We consider two clouds: one cloud is the extension of the other (the cloud described with the orange color is the extended version of the blue one). Both clouds extend below the $\tau = 1$ line (dashed line). The cloud illustrated in orange requires a higher molecular concentration (in this case NH_3) to reach a higher density in the lower layer. The right panel of Figure 5 shows the albedo that results from the cloud structure scenarios. The difference between the two models is significant and is due to higher scattering from the denser layer of the model in orange, but also to higher absorption from NH_3 in the gas phase, as it increases more than two orders of magnitude (the solely NH_3 absorption feature is around 0.64 μm).

By using the VMR profile to define the cloud structure (Figure 1), we can estimate the depth of the clouds as well as the VMR of the studied molecule before it condenses. For the test case and the arguments presented in this section, we expect a correlation between the $D_{\rm cld}$ and the molecular VMR below the clouds.

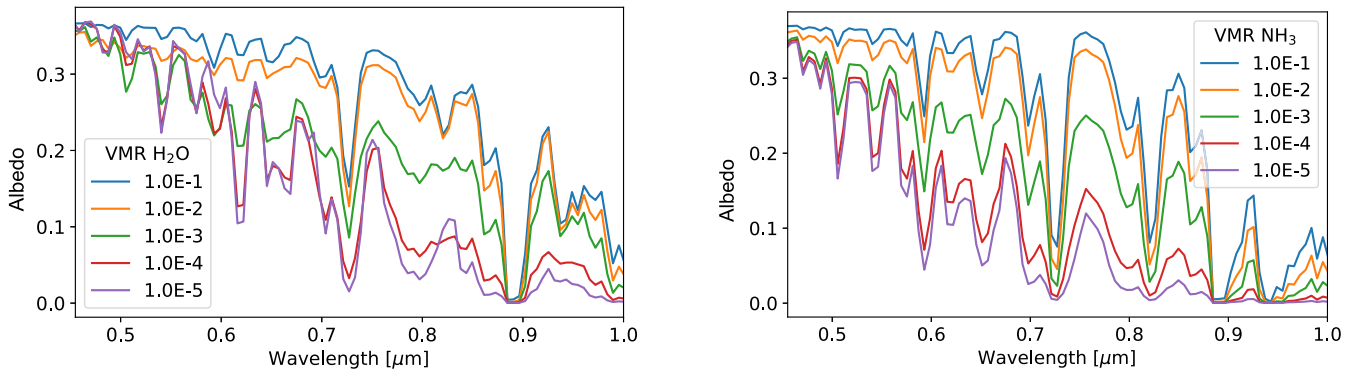

Figure 4. Left panel: the effect on the albedo due to the variation of the VMR of the water. Only a water cloud has been considered. Right panel: same as left panel but relative to the ammonia. Only an ammonia cloud has been included. For both graphs, we used $\log(\mathrm{VMR}_{\mathrm{CH_4}}) = -2.8$ $g = 50$ m s^{-2}. Also, the P_{top}, D_{cld}, and CR are the same, but relative to two different models: $\log(P_{\mathrm{top}}\ [\mathrm{Pa}]) = 4.0$, $\log(D_{\mathrm{cld}}\ [\mathrm{Pa}]) = 5.5$, and $\log(\mathrm{CR}) = -8.0$. The spectral resolution is $R = 70$, and the phase angle is $\alpha = 60°$.

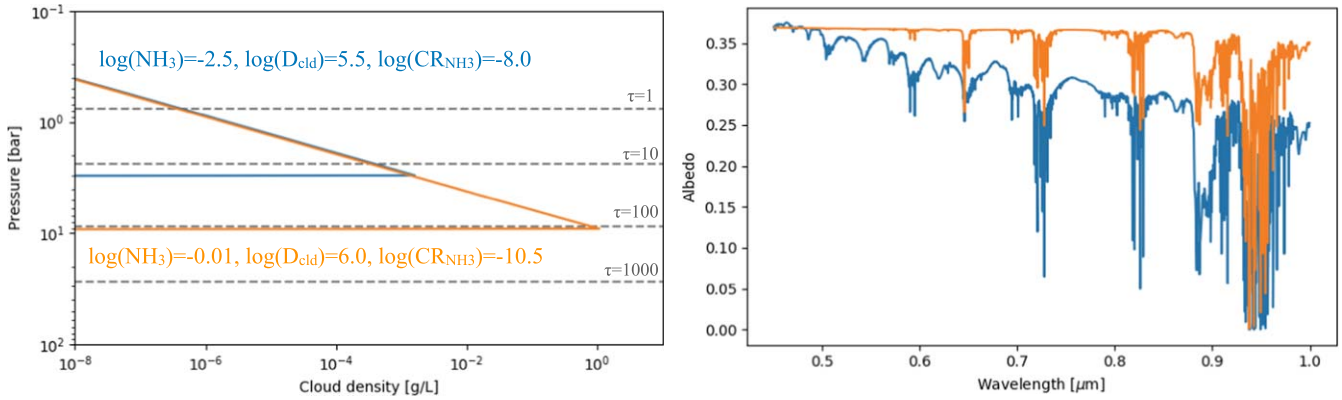

Figure 5. Left panel: cloud structure for the test case. The orange cloud is an extension of the blue cloud. The two models have the same values for the other parameters not reported in figure: $\log(\mathrm{VMR}_{\mathrm{H_2O}}) = -4.0$, $\log(\mathrm{VMR}_{\mathrm{CH_4}}) = -4.0$, $\log(P_{\mathrm{top}}) = -4.0$, $g = 50$ m s^{-2}. Right panel: the albedo resulting from considering the cloud structure on the left panel. The colors between the two panels are related. The orange cloud results in a higher reflectivity; however, more NH_3 is required to define such a cloud.

3.5. Clouds: H_2O versus NH_3

The setup used in this work to define the atmospheric vertical cloud distribution allows us to identify different types of clouds chemically. Depending on which VMR, either H_2O or NH_3, is modified, different types of clouds are calculated with particular cloud properties (e.g., single scattering albedo). In this section, we wanted to test if the cloud chemical composition difference can also be observed in terms of the planetary albedo spectrum. To test this hypothesis, we artificially constructed three different test cases (Figure 6). We simulated three artificial atmospheric scenarios for a Jupiter-like gas giant. First, we synthesized the atmospheric albedo spectrum (black curve on the right panel of Figure 6) resulting from the presence of a water cloud at around 0.1–1 bar and constant VMR for NH_3 and CH_4 (top left panel of Figure 6). Second, we switched the role of ammonia and water by mirroring the values used for the first case (middle right panel of Figure 6). This case is unrealistic, as the condensation of NH_3 implies the one of H_2O (ammonia condenses at lower temperature), so the VMR of water should be lower in the higher part of the atmosphere. However, as proof of concept, the resulting albedo of the second scenario (blue curve on the right panel of Figure 6) is noticeably different from the first case, mostly in the red part of the spectrum. This is because in the second case, the water VMR is high across the atmosphere resulting in stronger water absorption bands. Finally, we simulated a more realistic third case (bottom left panel of Figure 6) in which the NH_3 cloud structure is the same as the one used in the second scenario, but the water is now at a realistically lower VMR (similar to the one obtained in the first case above the water cloud). Even in this scenario, the resulting albedo spectrum shows differences at longer wavelengths (red curve on the right panel of Figure 6). The absorption due to water is now weak, and the albedo values at about 0.82 and 0.95 μm are high.

By analyzing these three cases, it is then possible, in principle, to discriminate between the different scenarios and cloud structures. However, it is essential to underline that the algorithm presented in this work is used as a forward model for a Bayesian sampler that always finds the best set of parameters that produce the best model to approximate the data. For this reason, we want to point out that an intermediate scenario between cases 2 and 3 (middle and bottom right panels of Figure 6) could be indistinguishable from case 1. However, the resulting VMR of water would be too high to be physically possible. This degeneracy can be ruled out by inferring other information from the model, e.g., the temperature of the planet, as the ammonia condenses at a lower temperature than the water.

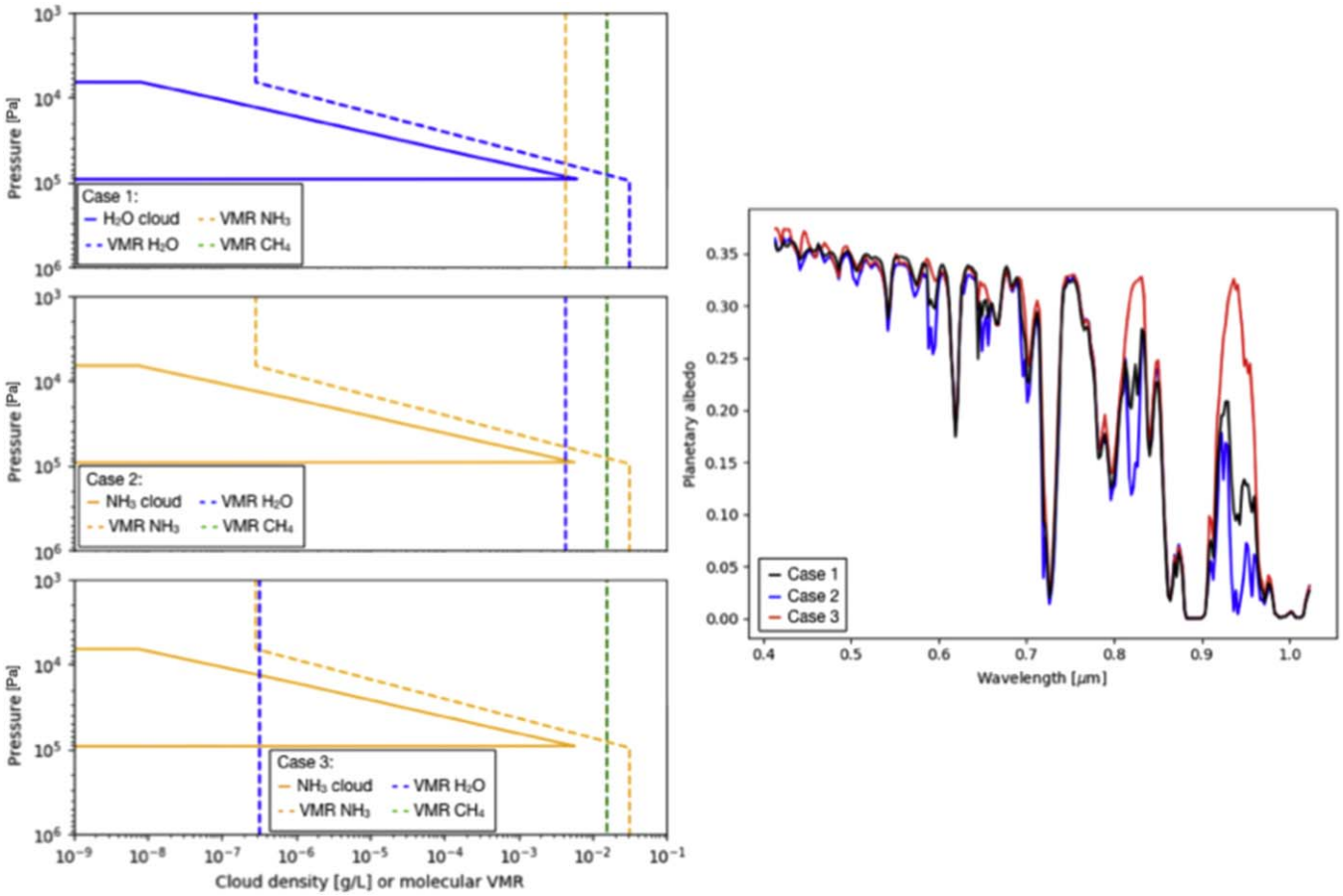

Figure 6. Left panels: the three different scenarios adopted to show the differences in the planetary albedo spectrum between the water and ammonia clouds. The top panel shows a water cloud vertical profile with constant ammonia and mathane VMR. The middle and bottom panels are referred to as the ammonia-cloud scenarios but with different constant water VMR value. Right panel: the resulting atmospheric albedo spectrum for each of the three scenarios in the left panels.

Table 2
Relevant Parameters Used in the Model for the υ And e Scenario

Stellar parameter	υ And
$R_\star$ ($R_\odot$)	1.56 ± 0.01[a]
$T_{\rm eff}$ (K)	6100 ± 80[a]
Planetary parameters	**(υ And e)**
$M_p \times \sin(i)$ ($M_{\rm Jup}$)	1.059 ± 0.028[b]
a (au)	5.24558 ± 0.00067[b]
e	0.00536 ± 0.00044[b]
$T_{\rm internal}$ (K)	110[c]
α (rad)	1.0472[c]

Notes.
[a] Butler et al. (1999).
[b] Curiel et al. (2011).
[c] Assumed.

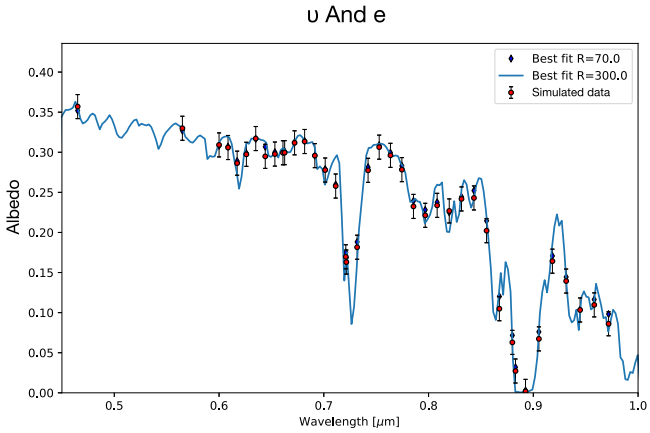

Figure 7. Albedo-wavelength dependence for the simulated planet υ And e. The red points represent the planetary albedo with a resolution of $R = 70$ and an S/N = 20. The ExoRel$^{\mathfrak{R}}$ best-fit model is also plotted ($R = 300$ blue line, and $R = 70$ blue diamond).

4. Result: Exoplanet Scenarios

4.1. υ And e

ExoRel$^{\mathfrak{R}}$ has been initially tested on synthesized data. We simulated the υ And e scenario (Butler et al. 1999; Curiel et al. 2011), which is a cold-Jupiter planet. It is one of the most Jupiter-like exoplanets found in terms of mass ($M \times \sin(i) = 1.059\, M_{\rm Jup}$) and semimajor axis (5.2456 au) (see Table 2). But orbiting a star larger than the Sun, it receives the same irradiation as a planet at 2.8 au in the solar system. The wavelength dependence of the albedo of this planet is expected to be mostly dominated by the methane absorption and deep water cloud presence (see Figure 7). For this reason, we synthesized the data point with values reported

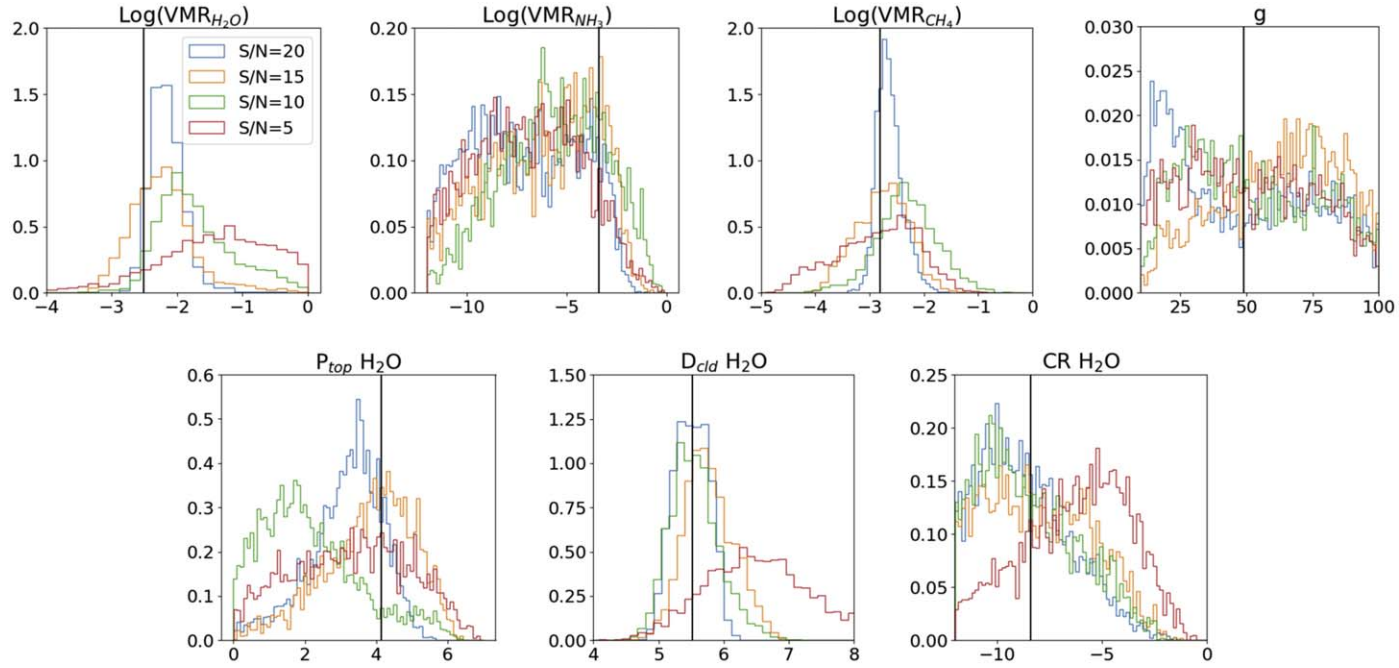

Figure 8. Marginalized distribution of the retrieved parameters at different S/Ns. The example is relative to the water cloud model; however, similar results are obtained with the ammonia-cloud model.

Table 3
Retrieval Results for υ And e as a Function of S/N

Parameter	Input	S/N = 5	S/N = 10	S/N = 15	S/N = 20
Log(VMR_{H_2O})	−2.51	$-1.39^{+1.28}_{-2.58}$	$-1.82^{+1.46}_{-0.77}$	$-2.26^{+1.36}_{-0.80}$	$-2.18^{+0.61}_{-0.40}$
Log(VMR_{NH_3})	−3.37	$-6.98^{+4.86}_{-4.55}$	$-5.64^{+4.39}_{-5.04}$	$-6.02^{+3.85}_{-5.48}$	$-7.20^{+4.59}_{-4.35}$
Log(VMR_{CH_4})	−2.81	$-2.79^{+1.20}_{-1.59}$	$-2.32^{+1.14}_{-1.20}$	$-2.75^{+0.91}_{-0.96}$	$-2.66^{+0.59}_{-0.37}$
g	48.97	$50.29^{+44.88}_{-37.18}$	$48.86^{+47.08}_{-33.61}$	$64.26^{+32.65}_{-46.58}$	$45.75^{+49.84}_{-33.55}$
Log(P_{top,H_2O})	4.14	$3.34^{+2.80}_{-2.98}$	$1.91^{+3.55}_{-1.75}$	$3.97^{+1.82}_{-2.95}$	$3.31^{+1.53}_{-2.59}$
Log(D_{cld,H_2O})	5.52	$6.51^{+1.82}_{-1.50}$	$5.53^{+0.91}_{-0.65}$	$5.74^{+0.83}_{-0.68}$	$5.50^{+0.48}_{-0.50}$
Log(CR_{H_2O})	−8.39	$-5.95^{+3.99}_{-5.36}$	$-8.85^{+5.25}_{-2.95}$	$-8.15^{+4.88}_{-3.60}$	$-8.91^{+4.91}_{-2.88}$
ln $\mathcal{Z}$		68.0 ± 0.3	92.3 ± 0.1	102.8 ± 0.2	116.9 ± 0.2

Note. The table also reports the median and 1σ uncertainties for the marginalized distribution of the listed parameters.

in the "Input" column of Table 3. The error bars have been calculated by considering a particular signal-to-noise ratio (S/N; e.g., 15, 20, etc.) with respect to the difference between the albedo continuum and the bottom of the strongest methane absorption band at ∼0.9 μm.

For the information retrieval process, we set uniform priors to the parameters listed in Table 1 relative to the water cloud case scenario.

We then run ExoRel$^{\mathfrak{R}}$ on the planetary albedo by fitting only water clouds. The marginalized distribution of the free parameters of the model is reported in Appendix A.1. We have been able to not only detect and quantify the amount of methane in the atmosphere, but we also recovered quantitative information about the concentration of water before its condensation level. The resulting gravity is unconstrained, as it does not affect the total albedo of the planet (see Section 3.1). Finally, the water cloud is located between $10^{3.45}$ and $10^{5.55}$ Pa with a strong CR that led the VMR of water on top of the cloud to be about 10^{-11}. The results shown in Appendix A.1 and reported in Table 3 led to a pressure level where the optical depth reaches unity ($\tau = 1$) to 10^5 Pa (1 bar). By looking at the marginalized distribution, we noted a weak correlation between the VMR of water and the cloud parameters as well as methane concentration with P_{top}, as expected. Overall, no strong correlations have been found across free-parameter space.

Additionally, we have used ExoRel$^{\mathfrak{R}}$ to perform an S/N analysis to observe the performance on the retrieved parameters (see Table 3 and Figure 8). We calculated the error bars at different S/Ns relative to the baseline. At S/N = 5, we noticed that no constraints can be determined. At this S/N, we only have weak information about the presence of methane in the atmosphere. At S/N = 10, we have a weak detection of water below the clouds and how much water has condensed, but it is not enough to quantitatively constrain these parameters. There is also a marginal quantification of methane content in the atmosphere, and the cloud depth is constrained. S/N = 15 presents a similar scenario with water (VMR and CR) and methane weakly constrained and the cloud depth quantified. At

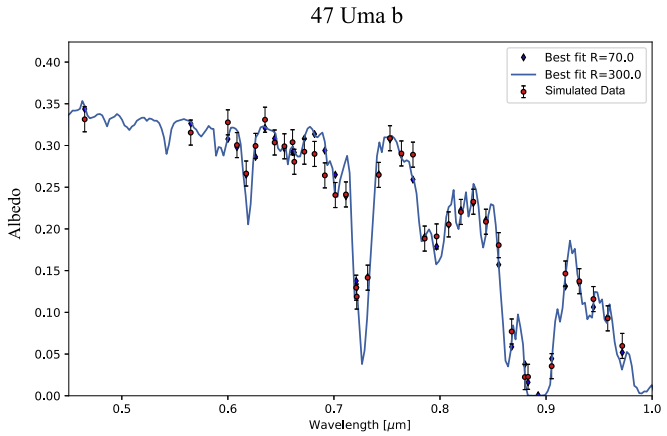

Figure 9. Best-fit models to the 47 Uma b simulated data. The data have a spectral resolution of $R = 70$, and the best-fit models are shown at $R = 300$ (solid blue line) and $R = 70$ (blue diamond).

Table 4
Relevant Parameters Used in the Model for 47 Uma b

Stellar parameter	47 Uma
$R_\star$ ($R_\odot$)	1.24 ± 0.04[a]
$T_{\rm eff}$ (K)	5892 ± 70[a]
Planetary Parameters	**47 Uma b**
M_p ($M_{\rm Jup}$)	2.53 ± 0.07[b]
a (au)	2.1 ± 0.02[b]
e	0.032 ± 0.014[b]
g (m s^{-2})	27.8750[c]
$T_{\rm internal}$ (K)	110[c]
α (rad)	1.0472[c]

Notes.
[a] Fuhrmann et al. (1997).
[b] Butler & Marcy (1996).
[c] Assumed.

S/N = 20, the results get much better with detection of most of the parameters (except for gravity, which does not play a significant role in the albedo modulation) with most of them also constrained (e.g., H_2O, CH_4, $P_{\rm top}$ and $D_{\rm cld}$). NH_3 has narrow absorption bands in the probed wavelength range, and for this reason, it is difficult to constrain it completely.

We have also tried to retrieve information from the spectrum by excluding the bluest points of the spectrum (data points with $\lambda < 0.6\,\mu$m). We did not notice significant shifts from the results presented before.

4.2. 47 Uma b

One of the exoplanets that is most likely to be observed by *WFIRST* for spectroscopic studies is 47 Uma b (Butler & Marcy 1996). It is a cold-Jupiter planet orbiting a sunlike star (G0V) at 2.1 au (see Table 4). With respect to the Jupiter–Sun system or the υ And e case, 47 Uma b (as it is closer to its host star) has a higher equilibrium temperature. In terms of cloud structure, this means that the upper atmosphere of the planet is expected to contain water clouds, as opposed to the ammonia clouds typical of Jupiter (Sudarsky et al. 2000). We used our self-consistent model (Hu 2019) to simulate the cloud structure. The simulated scenario agrees with the upper water clouds and absence of ammonia condensates. We interpolated the albedo in

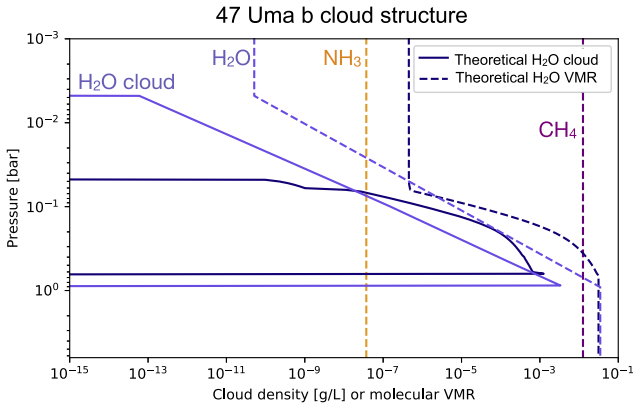

Figure 10. The dark blue lines show the theoretical water cloud structure and theoretical VMR vertical profile of water synthesized by using our self-consistent model (Hu 2019). The light blue lines show the retrieved cloud structure (solid line) and the water VMR (dashed line). The VMR of ammonia (orange dashed line) and methane (purple dashed line) have been considered constant across the atmosphere.

Table 5
Retrieval Results for 47 Uma b

Parameter	Input	Results
$\log(\mathrm{VMR}_{H_2O})$	-1.50	$-1.46^{+1.15}_{-0.43}$
$\log(\mathrm{VMR}_{NH_3})$	-2.37	$-7.43^{+5.14}_{-4.22}$
$\log(\mathrm{VMR}_{CH_4})$	-1.80	$-1.90^{+0.51}_{-0.52}$
$\log(P_{\mathrm{top},H_2O})$	3.36	$2.70^{+1.93}_{-2.32}$
$\log(D_{\mathrm{cld},H_2O})$	4.84	$4.99^{+0.40}_{-0.26}$
$\log(\mathrm{CR}_{H_2O})$	-4.84	$-8.83^{+5.63}_{-2.98}$

Note. The table reports the median and 1σ uncertainties for the marginalized distribution of the listed parameters alongside the input parameters used to synthesize the data.

the same wavelength grid used for the υ And e scenario (Section 4.1), in which we considered an S/N of 20, and we added the error bars to the data points according to the chosen S/N. We then used our framework to fit water clouds only to the simulated data (Figure 9). The input parameters used to synthesize the data and the resulting values are reported in Table 5. The marginalized distributions of the process are reported in Appendix A.2, and the theoretical and retrieved cloud structure is shown in Figure 10. Bayesian sampling was able to retrieve and quantify the cloud extension ($D_{\rm cld}$), the VMR of methane, and the VMR of the water in the deep layers of the atmosphere. There is a weak correlation between VMR_{CH_4} and $D_{\rm cld}$. The median values and the errors of the marginalized distribution agree with the true value used to synthesize the albedo with the exception of the VMR of ammonia (not enough NH_3 bands in the wavelength range) and the CR of the water. However, the retrieved CR_{H_2O} value ensures that on top of the clouds, the water concentration drops substantially; in this way, the water absorption is absent. The $P_{\rm top}$ marginalized distribution is broad, as the less dense part of the cloud (i.e., the top part) is difficult to constrain. However, its retrieved distribution is fairly consistent with the input value.

5. Result: Jupiter Test Case

Most of the models used to explain the observation of hot exoplanets relied entirely on theoretical consideration, as in the solar system these kind of planets are not present. In the case of

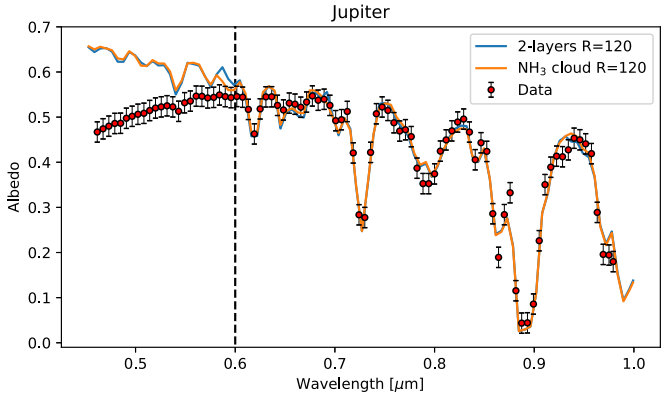

Figure 11. Best-fit models to the Jupiter albedo data (Karkoschka 1998). The continuous lines are relative the different cloud models: blue for the two-cloud model and orange for the ammonia-cloud model. The data have been reduced to spectral resolution $R = 120$, and the best-fit models are also reported at $R = 120$. Data with wavelengths lower than the vertical black dashed line have been excluded during the retrieval process.

Table 6
Retrieval Results for Jupiter

Parameter	Two-cloud	NH_3 Cloud
$\mathrm{Log}(\mathrm{VMR}_{H_2O})$	$-4.63^{+3.29}_{-2.34}$	$-6.64^{+0.43}_{-4.22}$
$\mathrm{Log}(\mathrm{VMR}_{NH_3})$	$-3.65^{+0.27}_{-0.21}$	$-3.54^{+0.24}_{-0.22}$
$\mathrm{Log}(\mathrm{VMR}_{CH_4})$	$-3.65^{+0.27}_{-0.23}$	$-3.54^{+0.25}_{-0.19}$
$\mathrm{Log}(P_{\mathrm{top},NH_3})$	$1.60^{+2.51}_{-1.50}$	$1.38^{+2.35}_{-1.18}$
$\mathrm{Log}(D_{\mathrm{cld},NH_3})$	$6.32^{+0.45}_{-0.34}$	$6.19^{+0.25}_{-0.26}$
$\mathrm{Log}(\mathrm{CR}_{NH_3})$	$-3.49^{+2.01}_{-3.35}$	$-3.64^{+1.89}_{3.40}$
$\mathrm{Log}(P_{\mathrm{top},H_2O})$	$3.67^{+3.22}_{-3.40}$	
$\mathrm{Log}(D_{\mathrm{cld},H_2O})$	$3.72^{+3.06}_{-3.48}$	
$\mathrm{Log}(\mathrm{CR}_{H_2O})$	$-5.37^{+4.17}_{6.15}$	
$\ln \mathcal{Z}$	135.8 ± 0.1	134.6 ± 0.1

Note. The table reports the median and 1σ uncertainties for the marginalized distribution of the listed parameters.

temperate/cold planets, we can test our model on realistic observations before applying them to exoplanetary observations. The scenario of the gaseous-giant planets (Jupiter and Saturn) in our solar system is within the scope of the model presented in this work. In this section, we present the results of the information retrieval analysis on Jupiter recorded by Karkoschka (1998). This also gives us the possibility to present and discuss the two-cloud versus one-cloud model.

The largest among the solar system's planets has been the object of deep studies to understand the composition and structure of its atmosphere (Weidenschilling & Lewis 1973; Sato & Hansen 1979; Karkoschka 1994, 1998; Simon-Miller et al. 2001; Wong et al. 2004; Sato et al. 2013). In the literature, the Jupiter cloud structure is defined respectively from the highest to the lowest in the atmosphere in terms of altitude, by NH_3, NH_4SH, and H_2O clouds positioned between 1 and 10 bars (Weidenschilling & Lewis 1973; Sato & Hansen 1979). In those works, NH_3 and NH_4SH clouds are expected to be enough to describe the observations. This makes Jupiter a suitable candidate to explore the performance of our two-cloud model (in this case, we can fit only ammonia and water clouds). We adopted Jupiter's albedo measured by Karkoschka (1998). The phase angle relative to those observations is $\alpha = 6.^{\circ}8$. We

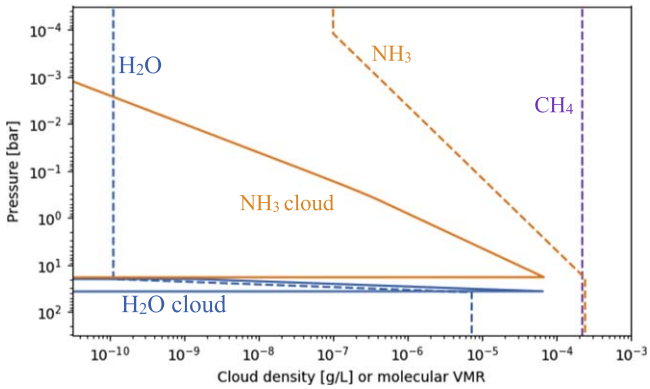

Figure 12. Retrieved atmospheric vertical profile of Jupiter. The values used to compute this graph are relative to the maximum likelihood of each parameter shown in the posterior distribution (Figure 15). The volume mixing ratios of the trace gasses are represented by the dashed lines, while the clouds are represented by continuous lines.

reduced the resolution to $R = 120$ and added error bars in agreement with an $S/N = 20$ relative to the baseline of the albedo. We then used this albedo to feed our algorithm and try to retrieve information from it.

We ran ExoRel$^{\mathfrak{R}}$ on Jupiter's albedo with the two-cloud model and with the ammonia-cloud-only model in two different instances. We calculated the Bayesian factor (see Section 2.3) associated with these two models ($\ln(\mathcal{B}_{\frac{\text{2-clouds}}{\text{NH3-cloud}}}) = 1.2$), and the preference toward the two-cloud model is not significant, as the ammonia clouds alone can explain most of the spectral information (see Figure 11).

The results of the retrieval are reported in Table 6, and the posterior distribution are reported in Appendices A.3 and A.4. For completeness, we report both the two-cloud model and ammonia-cloud posteriors because the preference toward one or the other model is not significant. The two posteriors are indeed similar in some aspects. From the retrieval, we obtained a quantification of ammonia and methane with a ratio $CH_4/NH_3 \sim 1$. The ammonia concentration, however, drops above the clouds to about 10^{-7}. The log-concentration of methane has been recovered as $-3.65^{+0.27}_{-0.23}$ for the two-cloud model and as $-3.54^{+0.25}_{-0.19}$ for the ammonia-cloud-only model. The reported error bar corresponds to 1σ confidence. If we consider 3σ, the methane concentration values are in agreement with the value reported in Wong et al. (2004) and other retrieval work (Lupu et al. 2016) in which the process has been performed on Jupiter data taken from Karkoschka (1994). We found a multimodal solution for the concentration of water, probably due to the not-so-high significance of the two-cloud model. The depth of the water cloud is not significant, making the cloud too thin, which is the reason why there is not much difference between the two-cloud model and the NH_3 cloud model.

The cloud's retrieved position (see Table 6 and Figure 12) is, in general, in agreement with the theorized atmospheric structure of Jupiter being between 1 and 20 bars (Weidenschilling & Lewis 1973; Sato & Hansen 1979). However, the actual structure is much more complex than the one that we obtained, with NH_4SH clouds and different haze layers (West et al. 1986).

We noticed, however, some correlations among the free parameters; the strongest is the one between the retrieved value of ammonia below the clouds and the concentration of methane. This is a consequence of the correlations of these

two parameters with the depth of the ammonia cloud. Both the abundance of ammonia and the depth affect the density of the clouds (see Section 3.4). The correlation between the methane VMR and the cloud position is also well known in previous works (Irwin et al. 2015; Lupu et al. 2016).

6. Discussion

Reflection spectroscopy is an emergent topic, and for this reason, different retrieval models have been proposed and tested. Regarding cold gaseous planets, a few models have been published (Lupu et al. 2016; Nayak et al. 2017; Batalha et al. 2019; Lacy et al. 2019). One of these models (Lacy et al. 2019) is inspired by empirical observations, but the free parameters are not necessarily linked to physical quantities. The other models agree on having the single scattering albedo ($\bar{\omega}$), the asymmetry factor ($\bar{g}$), and the optical depth (τ) within their free parameters, as the cloud model is not linked to a physical model of cloud structure (e.g., particle size and chemical identity of cloud constituents are not taken into account).

In this work, we wanted to follow some of the other models' aspects and eventually propose a different point of view. For the interpretation of hot-Jupiter observations, we could not gain insight from observations in the solar system, as it lacks these types of planets. For cold gaseous planets, it is different: we can observe them closely with much more detail and take inspiration for developing general models.

Weidenschilling & Lewis (1973) and Atreya et al. (1999) have successfully predicted the bulk cloud structure of Jupiter by considering water and ammonia as condensable species. This fact has been implemented in our model, and we made a distinction between water and ammonia clouds as their physical properties are linked to the relative nonuniform molecular VMR vertical profile. However, the distinction between the two clouds given by the information retrieval of the spectrum depends on the case. The VMR of water and ammonia in the atmosphere is directly linked with the density of the corresponding cloud (Equation (2)); the more water or ammonia is present in the atmosphere, the more dense a cloud can be, affecting the optical properties of the cloud itself. Our cloud model is linked with a physical model that calculates cloud density and particle size. As presented in the literature, this is likely to bring a correlation between the VMR of methane and cloud position (Irwin et al. 2015; Lupu et al. 2016). However, there might be cases in which this correlation is not significant; as highlighted by Hu (2019), it depends on a combination of S/N, spectral resolution, and particular combinations of cloud positions and methane VMR.

6.1. The Role of P_{top} and D_{cld}

Unlike the common definition of $P_{\rm top}$ (Irwin et al. 2008; Madhusudhan & Seager 2009; Benneke & Seager 2012; Waldmann et al. 2015a, 2015b; Lupu et al. 2016; Feng et al. 2018; Batalha et al. 2019), in the algorithm presented here, it does not play a central role. The $P_{\rm top}$ regulates the least-dense part of the cloud where not much scattering is happening. This, in part, explains why we observe a broad posterior of $P_{\rm top}$ in our marginalized histograms. Most of the scattering happens at the bottom of the cloud where it is denser. $D_{\rm cld}$ is the parameter related to the lower part of the cloud where most of the scattering happens. Moreover, most of the time, the pressure value at which the optical depth reaches the unity ($P_{\tau=1}$) is close to the bottom of the cloud. Finally, since $P_{\rm bot}$ is defined as the sum of $P_{\rm top}$ and $D_{\rm cld}$, most of the time, $D_{\rm cld}$ will dominate the summation, making the posterior of $P_{\rm top}$ broader toward lower values. To compare our work to those in the literature, $D_{\rm cld}$ is the parameter in which the attention should be focused on.

6.2. Jupiter Results

Even though our model is inspired by solar system observations and by Weidenschilling & Lewis (1973) and Sato & Hansen (1979), there are assumptions and simplifications that create differences between the literature and our models. Jupiter's cloud structures theorized in the literature assume the presence of hazes and multiple (even more than two) cloud layers of different molecular species. In our model, instead, we did not include hazes. We have not modeled the condensation of NH_4SH, which could be necessary to have a better fit of Jupiter's and other scenarios of reflected spectra.

The results we obtained for Jupiter (Table 6, Figures 11 and 12) show that a single cloud layer can be sufficient to explain the albedo modulation. However, since we have the sensibility to differentiate cloud species, using a two-cloud model configuration with NH_3 and NH_4SH condensates and the presence of hazes may have a better outcome than the water cloud, which does not really contribute to the albedo modulation. The overall position of the NH_3 cloud reflects, however, the clouds position reported in Weidenschilling & Lewis (1973) and also the position of clouds measured by planetary missions (West et al. 1986). We want to point out that even if the theoretical values are used in the fully consistent model ExoRel (Hu 2019) and a theoretical cloud structure is considered, the calculated albedo, while it matches with Jupiter in its bulk part, cannot sufficiently account for the methane weak bands. This suggests that further effects need to be taken into account (Hu 2019). This may also explain why the concentration of methane has been underestimated by our model. However, we would like to point out that even though these simplifications have been adopted, our recovered free-parameter values agree with the literature works within 3σ confidence.

Bayesian samplers are designed to explore the parameter space to find the solution that best approximates the data. The result of this process will closely reflect reality only if most of the effects that take place in the process under study are taken into account. In this sense, hazes, other absorbers, and cloud species may be required for future studies.

6.3. Water versus Ammonia Clouds

In Section 2.1, we described the steps required for the atmospheric structure to be constructed. We differentiated water clouds from ammonia clouds by considering different VMR vertical profiles for the two molecules and different particle sizes (as we used the mean molecular mass for the calculation). Also, the opacities of the two molecules are different, and this creates a further distinction between the two cloud species when the single scattering albedo is calculated.

In Section 3.5, we synthesized three different scenarios to try to distinguish between water and ammonia clouds. However, whether or not we are able to distinguish between the two species with this algorithm will be case-dependent. By

combining information from the Bayesian factor, the expected temperature of the planet, and the use of the self-consistent model, we might be able to discriminate between the two cloud species. The results of the Bayesian sampling could indeed be compared with a self-consistent model and used to determine if the two outcomes agree with each other.

6.4. Implication of Constraining the Molecular VMR below the Clouds

Direct quantification of molecular abundances below the cloud deck has been a difficult task. Most of the models in the literature that interpret atmospheric spectra do not quantify parameters below $P_{\tau=1}$ by design. In our work, we tried to link the presence of condensates to the variation of molecular concentration. This gave us the freedom to fit the concentration value below the clouds. Essentially, we are assuming that for a certain condensate to be present (defined by density, particle size, and extension, see Section 3.4), a particular non-constant VMR vertical profile is required. This assumption may have an important implication: in the cold gaseous planets scenario, it could help improve atmospheric modeling and detect the presence of water and ammonia unseen in direct measurements. This behavior is also embedded in our algorithm as the VMR of such molecules on top of the clouds drops drastically, making them almost undetectable.

6.5. Spectral Noise Realization

In this work, we showed a novel approach to modeling and retrieving chemical abundance and cloud information from cool gaseous-giant-planet spectra. For this reason, we focused on the description and performance of the model without stressing the aspect of the spectral noise. In the retrieval exercises presented in this work (Sections 4 and 5), we added error bars to the spectral data points by calculating the average albedo across the wavelength range and scaling it by the chosen S/N. This may lead to underestimating the retrieval error and introducing biases. Previous works (Lupu et al. 2016; Feng et al. 2018) have shown that accounting for a random noise increases the uncertainty of the retrieved values significantly as the data points are extracted from a Gaussian distribution that changes the value of each measurement away from a simple model mean. In this context, the results presented in this work are optimistic, and including a random noise to the data points would weaken the constraint on the retrieved values at high S/N (20 or 15) and completely fade out any quantitative detection at lower S/N (10 or 5).

7. Conclusion

In this work, we presented ExoRel$^{\mathfrak{R}}$, our novel Bayesian inverse retrieval algorithm for exoplanetary reflected light spectra. The gas giants' albedo (key ingredient of reflection spectroscopy) in the visible and near-infrared wavelength is mostly affected by cloud scattering and molecular absorption from H_2O, NH_3, and CH_4. We used a nonuniform VMR vertical profile of water and ammonia to construct water and ammonia clouds. Compared to previous retrieval models of reflected light spectra, ExoRel$^{\mathfrak{R}}$ enforces the causal relationship between the gas abundance and the corresponding cloud density. Since ExoRel$^{\mathfrak{R}}$ calculates the single scattering albedo, the asymmetry factor and the optical depth consistently, it employs a set of free parameters that define the nonuniform VMR of water and ammonia, e.g., the cloud depth ($D_{\rm cld}$) and the VMR below the clouds (see Figure 1). We presented the performances of our model with two exoplanetary test cases: υ And e and 47 Uma b, which are candidates to be observed and characterized by the upcoming *WFIRST* mission. Finally, we have run our algorithm on a realistic case by trying to analyze the Jupiter albedo.

The key results of our work comprise the evidence of cloud presence and position estimation, the physical characterization of clouds (cloud density and particle size profiles), possibility to determine cloud chemical constituent (distinction between water and ammonia clouds), and the quantification of methane concentration and possible indirect quantification of the VMR of condensable molecules below the cloud.

The retrieval exercises presented in this paper show that the reflected light spectra expected to be recorded by future space missions should be sufficient to put meaningful constraints on the presence of clouds and the abundance of methane. This conclusion is validated by the solar system test case, where we fit a relatively simple model to the Jupiter planetary atmosphere known to be complex. If the S/N is high enough, reflected light spectroscopy may help us quantify the cloud extension, which reflects the position of the clouds, as well as the below-cloud concentration of the gas responsible for the presence of the cloud itself.

For this initial instance, some approximations have been made (e.g., log-linear condensation of water and ammonia, and absence of hazes). In this work, we have focused on the possibility of retrieving parameters about the atmospheric characteristics of cold gaseous planets. In a future work, this algorithm will be further developed to also include temperate/cold rocky planet scenarios with H_2- and non H_2-dominated atmospheres.

The authors thank Dr. Graça M. Rocha and Dr. Sergi R. Hildebrandt for helpful discussions, materials, and encouragement in the preparation of this manuscript. This work was supported in part by the NASA *WFIRST* Preparatory Science grant #NNN13D460T, and NASA *WFIRST* Science Investigation Teams grant #NNN16D016T. The research was carried out at the California Institute of Technology Jet Propulsion Laboratory. This research was carried out at the Jet Propulsion Laboratory, California Institute of Technology, under a contract with the National Aeronautics and Space Administration.

Appendix
Posterior Distributions

A.1. υ And e—Water Cloud

Result of the Bayesian statistical analysis on the υ And e simulated spectrum. The posterior distribution is shown in Figure A.1.

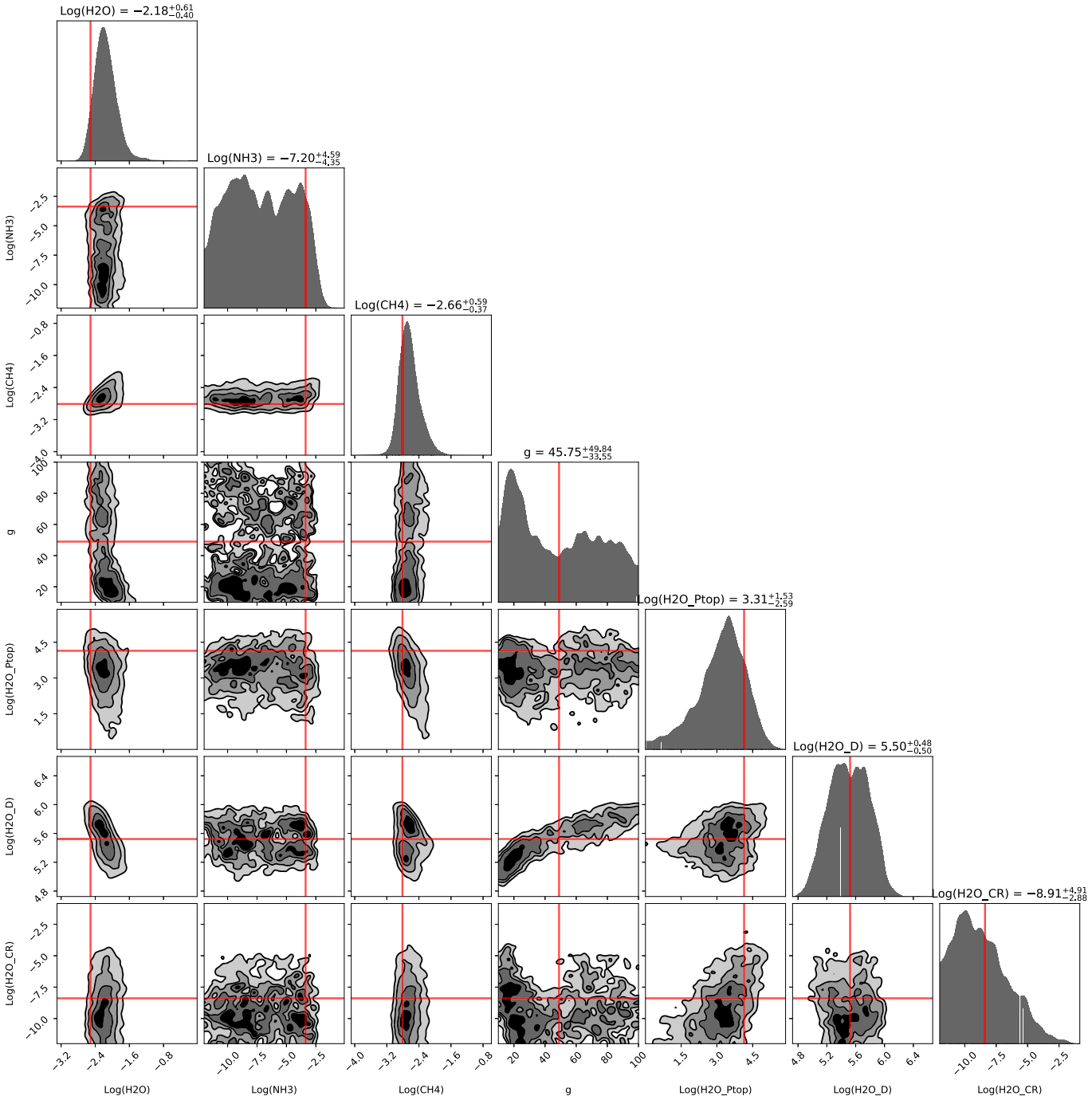

Figure A.1. Posterior distribution of the free parameters of the model for the υ And e scenario. The red lines indicate the ground truths of the synthesized model. The numbers reported on top of the 1D distributions are relative to the median and 1σ values of the distributions. The correlation between CH_4 and P_{top} is weak. In this example, the correlation between VMR_{H_2O} and both VMR_{CH_4} and D_{cld,H_2O} can be seen; however, the relative 2D distributions are quite localized. No multimodal solutions have been found.

A.2. 47 Uma b—Water Cloud

Result of the Bayesian statistical analysis on the 47 Uma b simulated spectrum. The posterior distribution is shown in Figure A.2.

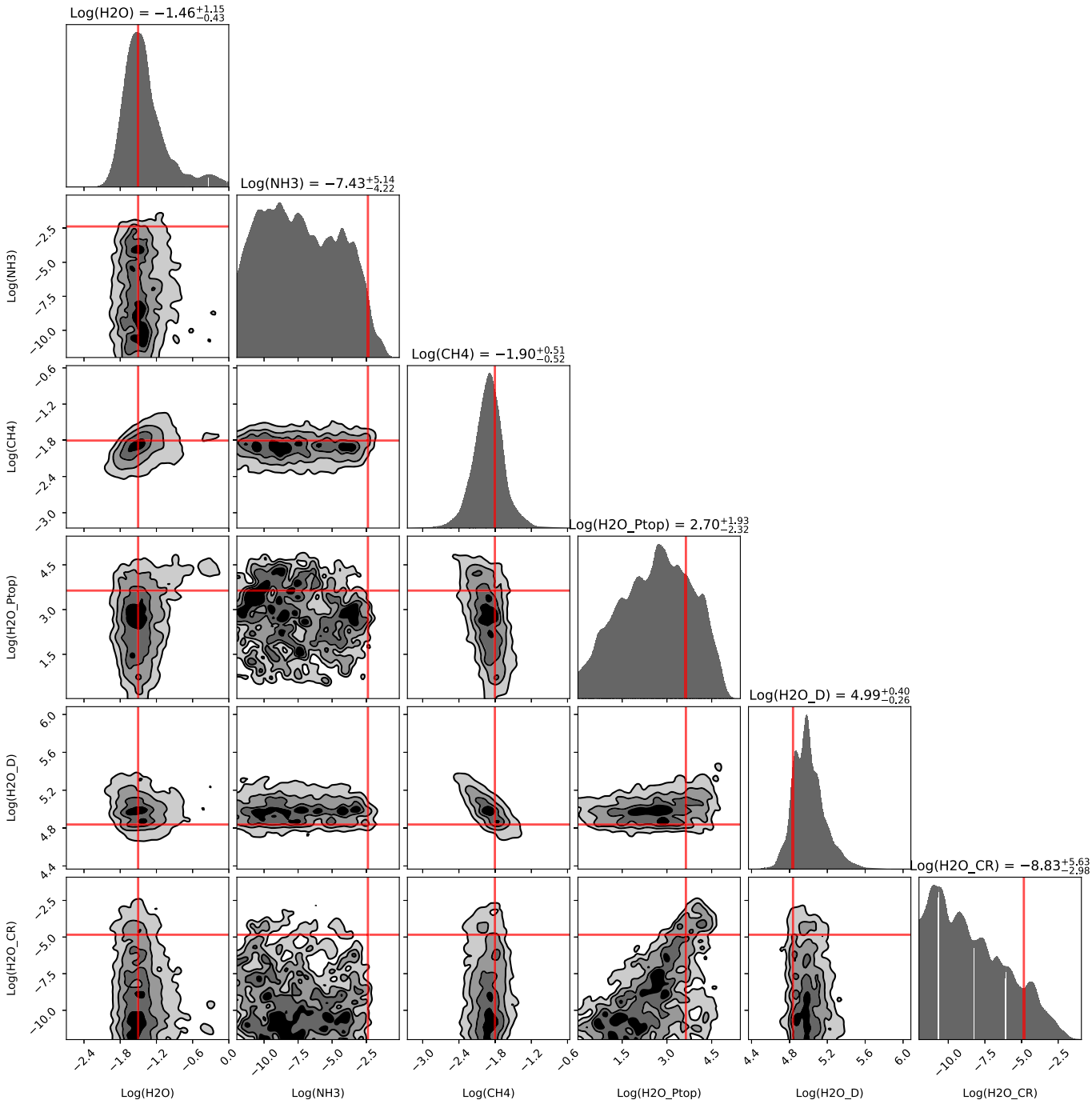

Figure A.2. Posterior distribution of the free parameters of the water model for the 47 Uma b science case. The numbers reported on top of the 1D distributions are relative to the median and 1σ values of the distributions. The solid red lines refer to the input parameters (ground truths) used to synthesize the data.

A.3. Jupiter (♃)—Two-cloud Model

Result of the Bayesian statistical analysis on the Jupiter binned spectrum. The ExoREL$^{\mathfrak{R}}$ model used here is relative to the two-cloud model. The posterior distribution is shown in Figure A.3.

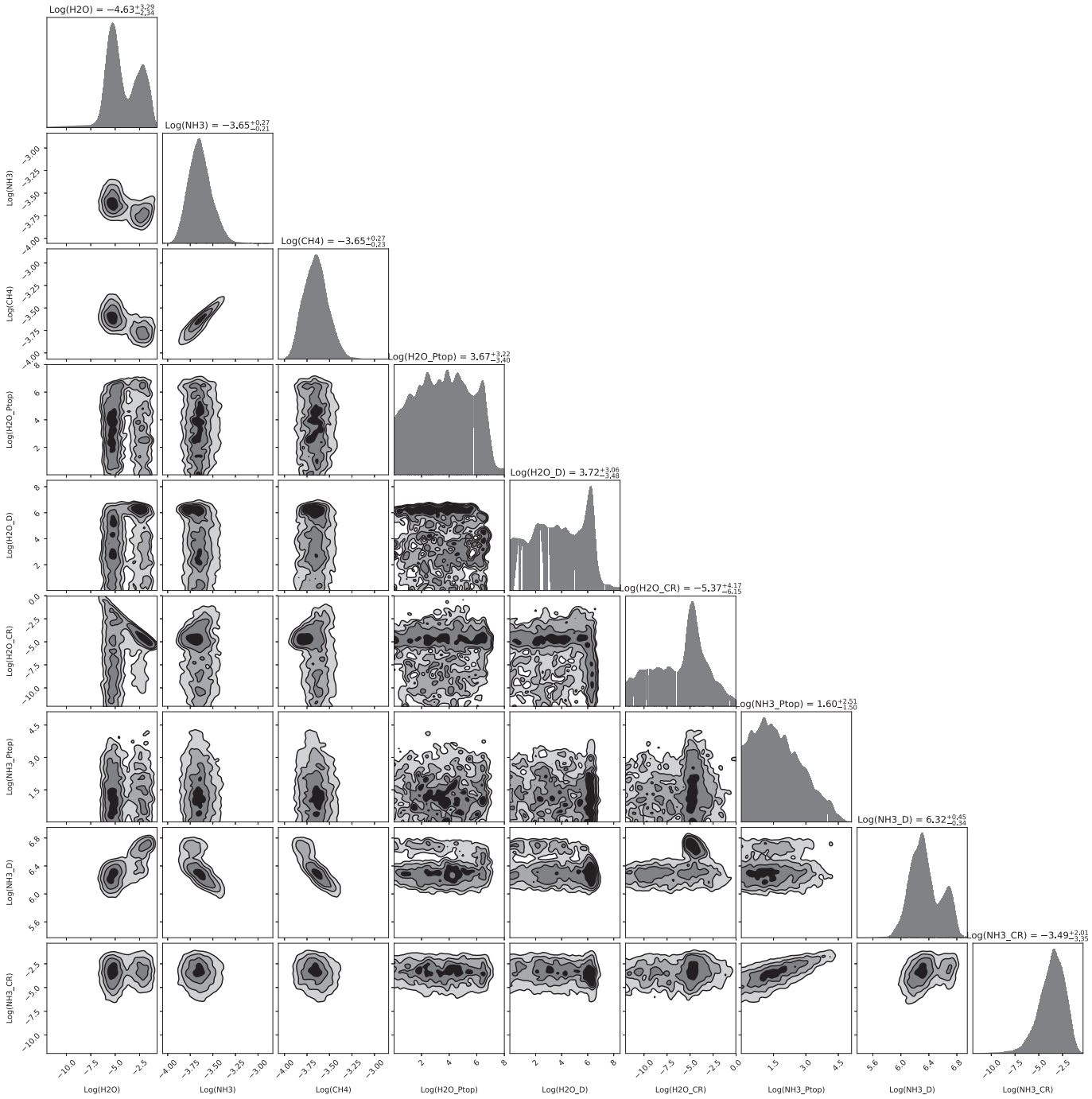

Figure A.3. Posterior distribution of the free parameters of the two-cloud model for the Jupiter scenario. The numbers reported on top of the 1D distributions are relative to the median and 1σ values of the distributions.

A.4. Jupiter (2)—Ammonia Cloud

Result of the Bayesian statistical analysis on the Jupiter binned spectrum. The ExoRel$^{\mathfrak{R}}$ model used here is relative to the ammonia cloud model solely. The posterior distribution is shown in Figure A.4.

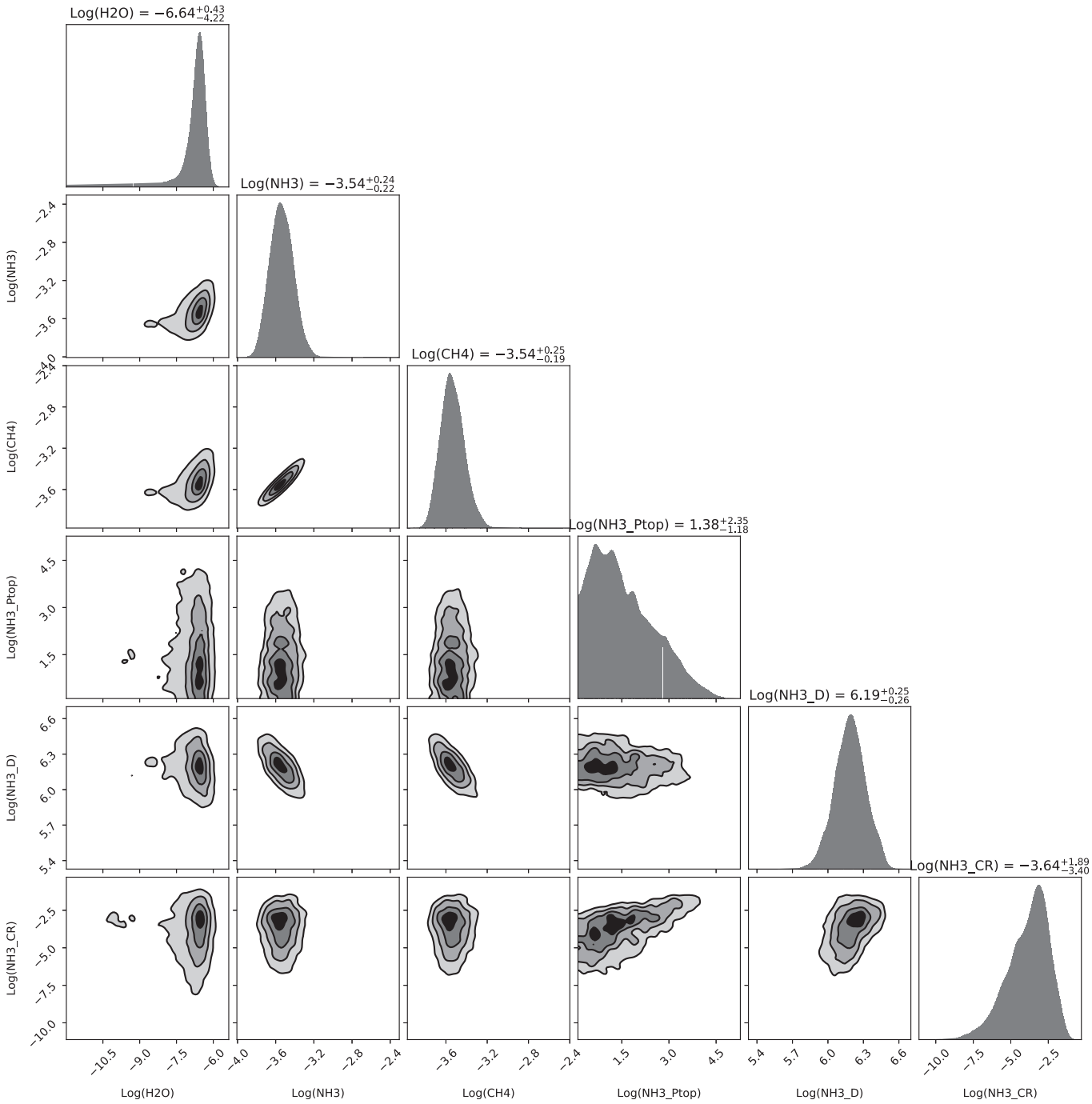

Figure A.4. Posterior distribution of the free parameters of the ammonia-cloud model for the Jupiter science case. The numbers reported on top of the 1D distributions are relative to the median and 1σ values of the distributions.

ORCID iDs

Mario Damiano https://orcid.org/0000-0002-1830-8260
Renyu Hu https://orcid.org/0000-0003-2215-8485

References

Ackerman, A. S., & Marley, M. S. 2001, ApJ, 556, 872
Atreya, S. K., Wong, M. H., Owen, T. C., et al. 1999, P&SS, 47, 1243
Barman, T. S., Macintosh, B., Konopacky, Q. M., & Marois, C. 2011, ApJ, 733, 65
Barstow, J. K., Aigrain, S., Irwin, P. G. J., & Sing, D. K. 2017, ApJ, 834, 50
Batalha, N. E., Marley, M. S., Lewis, N. K., & Fortney, J. J. 2019, ApJ, 878, 70
Benneke, B., & Seager, S. 2012, ApJ, 753, 100
Berta, Z. K., Charbonneau, D., Désert, J.-M., et al. 2012, ApJ, 747, 35
Buchner, J., Georgakakis, A., Nandra, K., et al. 2014, A&A, 564, A125
Burrows, A. 2014, arXiv:1412.6097
Burrows, A., Marley, M., Hubbard, W. B., et al. 1997, ApJ, 491, 856
Burrows, A., Sudarsky, D., & Hubeny, I. 2004, ApJ, 609, 407
Butler, R. P., & Marcy, G. W. 1996, ApJL, 464, L153
Butler, R. P., Marcy, G. W., Fischer, D. A., et al. 1999, ApJ, 526, 916
Cahoy, K. L., Marley, M. S., & Fortney, J. J. 2010, ApJ, 724, 189
Curiel, S., Cantó, J., Georgiev, L., Chávez, C. E., & Poveda, A. 2011, A&A, 525, A78
Damiano, M., Micela, G., & Tinetti, G. 2019, ApJ, 878, 153
Damiano, M., Morello, G., Tsiaras, A., Zingales, T., & Tinetti, G. 2017, AJ, 154, 39

Evans, T. M., Sing, D. K., Wakeford, H. R., et al. 2016, ApJL, 822, L4
Feng, Y. K., Robinson, T. D., Fortney, J. J., et al. 2018, AJ, 155, 200
Feroz, F., & Hobson, M. P. 2008, MNRAS, 384, 449
Feroz, F., Hobson, M. P., & Bridges, M. T. B. 2009, MNRAS, 398, 1601
Feroz, F., Hobson, M. P., Cameron, E., & Pettitt, A. N. 2019, OJAp, 2, 10
Fraine, J., Deming, D., Benneke, B., et al. 2014, Natur, 513, 526
Fuhrmann, K., Pfeiffer, M. J., & Bernkopf, J. 1997, A&A, 326, 1081
Hu, R. 2014, arXiv:1412.7582
Hu, R. 2019, ApJ, 887, 166
Irwin, P. G. J., Teanby, N. A., de Kok, R., et al. 2008, JQSRT, 109, 1136
Irwin, P. G. J., Tice, D. S., Fletcher, L. N., et al. 2015, Icar, 250, 462
Karkoschka, E. 1994, Icar, 111, 174
Karkoschka, E. 1998, Icar, 133, 134
Knutson, H. A., Benneke, B., Deming, D., & Homeier, D. 2014, Natur, 505, 66
Lacy, B., Shlivko, D., & Burrows, A. 2019, AJ, 157, 132
Lupu, R. E., Marley, M. S., Lewis, N., et al. 2016, AJ, 152, 217
MacDonald, R. J., Marley, M. S., Fortney, J. J., & Lewis, N. K. 2018, ApJ, 858, 69
Macintosh, B., Graham, J. R., Barman, T., et al. 2015, Sci, 350, 64
Madhusudhan, N., & Seager, S. 2009, ApJ, 707, 24
Marley, M., Lupu, R., Lewis, N., et al. 2014, arXiv:1412.8440
Marley, M. S., Gelino, C., Stephens, D., Lunine, J. I., & Freedman, R. 1999, ApJ, 513, 879
Mennesson, B., Gaudi, S., Seager, S., et al. 2016, Proc. SPIE, 9904, 99040L
Nayak, M., Lupu, R., Marley, M. S., et al. 2017, PASP, 129, 034401
Peterson, B. M., Fischer, D. & LUVOIR Science and Technology Definition Team 2017, AAS Meeting Abstracts, 229, 405.04
Sato, M., & Hansen, J. E. 1979, JAtS, 36, 1133
Sato, T. M., Satoh, T., & Kasaba, Y. 2013, Icar, 222, 100
Seager, S., & Sasselov, D. D. 1998, ApJL, 502, L157
Seager, S., Whitney, B. A., & Sasselov, D. D. 2000, ApJ, 540, 504
Simon-Miller, A. A., Banfield, D., & Gierasch, P. J. 2001, Icar, 154, 459
Sing, D. K., Fortney, J. J., Nikolov, N., et al. 2016, Natur, 529, 59
Sivia, D., & Skilling, J. 2006, Data Analysis A Bayesian Tutorial (Oxford: Oxford Univ. Press)
Skemer, A. J., Marley, M. S., Hinz, P. M., et al. 2014, ApJ, 792, 17
Skilling, J. 2004, in AIP Conf. Ser. 735, Bayesian Inference and Maximum Entropy Methods in Science and Engineering: 24th International Workshop on Bayesian Inference and Maximum Entropy Methods in Science and Engineering, ed. R. Fischer, R. Preuss, & U. V. Toussaint (Meville, NY: AIP), 395
Skilling, J. 2006, BayAn, 4, 833
Snellen, I. A. G., de Kok, R. J., de Mooij, E. J. W., & Albrecht, S. 2010, Natur, 465, 1049
Spergel, D., Gehrels, N., Baltay, C., et al. 2015, arXiv:1503.03757
Spergel, D., Gehrels, N., Breckinridge, J., et al. 2013, arXiv:1305.5422
Sudarsky, D., Burrows, A., & Hubeny, I. 2003, ApJ, 588, 1121
Sudarsky, D., Burrows, A., & Pinto, P. 2000, ApJ, 538, 885
Swain, M. R., Tinetti, G., Vasisht, G., et al. 2009, ApJ, 704, 1616
Swain, M. R., Vasisht, G., & Tinetti, G. 2008, Natur, 452, 329
Trotta, R. 2008, ConPh, 49, 71
Tsiaras, A., Waldmann, I. P., Zingales, T., et al. 2018, AJ, 155, 156
Waldmann, I. P., Rocchetto, M., Tinetti, G., et al. 2015a, ApJ, 813, 13
Waldmann, I. P., Tinetti, G., Rocchetto, M., et al. 2015b, ApJ, 802, 107
Weidenschilling, S. J., & Lewis, J. S. 1973, Icar, 20, 465
West, R. A., Strobel, D. F., & Tomasko, M. G. 1986, Icar, 65, 161
Wong, M. H., Mahaffy, P. R., Atreya, S. K., Niemann, H. B., & Owen, T. C. 2004, Icar, 171, 153